Coupled Protonic and Electronic Conduction in the Molecular Conductor [2-(2-1*H*-Benzimidazolyl)-1*H*-benzimidazolium] – TCNQ

Tomoyuki Akutagawa,*[a, b] Tatsuo Hasegawa,[a] Takayoshi Nakamura,*[a] Tamotsu Inabe,[c] and Gunzi Saito[d]

Abstract: A novel molecular based proton – electron mixed conductor, (H3BBIM$^+$)(TCNQ)(Cl$^-$)$_{0.5}$(H_2O) (**1**), where H3BBIM$^+$ is 2-(2-1*H*-benzimidazolyl)-1*H*-benzimidazolium and TCNQ is 7,7,8,8-tetracyano-*p*-quinodimethane, was synthesized. The salt exhibited peculiar phase transitions as a result of proton – electron coupling phenomena within the crystal. Salt **1** is composed of a closed-shell H3BBIM$^+$ cation and an open-shell TCNQ anion radical, and was obtained by electrocrystallization in a buffered CH_3CN solution. Crystal **1** was constructed from the segregated uniform stacks of H3BBIM$^+$ and TCNQ. The regular stack of partially electron-transferred TCNQ$^{-0.5}$ provided a one-dimensional electron-conducting column. Between the regular H3BBIM$^+$ columns, a channel-like sequence of holes was formed at the side-by-side space that is filled with disordered Cl$^-$ ions and H_2O molecules, and which offer a proton-conducting path. The electrical conductivity at room temperature (10 S cm^{-1}) was greater by a magnitude of four than the protonic conductivity (1×10^{-3} S cm^{-1}). Electronic conduction changed from metallic ($T > 250$ K) to semiconducting ($250 > T > 100$ K), then insulating ($T < 100$ K). Protonic conductivity was observed above 200 K. The continuous metal – semiconductor transition at 250 K is caused by the formation of the Cl$^-$ superstructure, whereas the disappearance of protonic conductivity at 200 K is related to the rearrangement of the [Cl$^-$ – (H_2O)$_2$] sublattice within the channel. The magnetic susceptibility continuously shifted from Pauli paramagnetism ($T > 250$ K) to the one-dimensional linear Heisenberg antiferromagnetic chain ($T < 250$ K). Lattice dimerization in regular TCNQ columns was confirmed by the appearance of vibrational a_g mode at low temperatures. The strong localization of conduction electrons on each TCNQ dimer caused a Mott transition at 100 K. The melting and freezing of the [Cl$^-$ – (H_2O)$_2$] sublattice within the channel was correlated to the conduction electrons on the TCNQ stack and the protonic conductivity.

Keywords: charge transfer · conducting materials · cooperative effects · electron transport · hydrogen bonds · proton transport · quinodimethanes

Introduction

The phenomenon of electron – proton coupling plays an important role in biological systems, such as the respiration and photosynthetic systems of photosynthetic bacteria, chloroplasts, and mitochondria.[1] Stepwise electron transfer from a special chlorophyll dimer, chlorophyll *B*, pheophytin, or quinone, to heme and/or ferredoxin has been recognized in photosynthetic systems,[2] while a proton transport (pump) mechanism has been recently elucidated from the X-ray crystal structure analysis of cytochrome *c* oxidase from the soil bacterium *Paracoccus denitrificans*.[3] In the case of cytochrome *c* oxidase, the transition metal ions of the heme molecule, Fe^{3+} and Cu^{2+}, are important ions within the redox active sites, and were shown to receive the electrons from ferredoxin; the reduced Fe^{2+} and Cu^+ ions then drive a proton pump through an electron – proton coupling.[3] During the proton path of cytochrome *c* oxidase, the 1*H*-imidazole (HIm)

[a] Dr. T. Akutagawa, Prof. T. Nakamura, Prof. T. Hasegawa
Research Institute for Electronic Science
Hokkaido University, N12W6 kita-ku
Sapporo 060-0812 (Japan)
Fax: (+81) 11-706-4972
E-mail: takuta@imd.es.hokudai.ac.jp

[b] Dr. T. Akutagawa
PRESTO, Japan Science and Technology Corporation
Kawaguchi 332-0012 (Japan)

[c] Prof. T. Inabe
Graduate School of Science, Hokkaido University
Sapporo 060-0810 (Japan)

[d] Prof. G. Saito
Graduate School of Science, Kyoto University, Kyoto 606-8502 (Japan)

Supporting information for this article is available on the WWW under http://www.chemeurj.org/ or from the author.

0947-6539/02/0819-4402 $ 20.00+.50/0 *Chem. Eur. J.* **2002**, *8*, No. 19

residue of histidine also plays an important role in accepting and donating protons through redox coupling. It was reported that the overall proton–electron couplings of Cu^{2+}(imidazolate$^-$) + e^- + $H^+ = Cu^+$(HIm) and Fe^{3+}(HIm) + e^- + $H^+ = Fe^{2+}$(imidazolium$^+$) transport the protons from the cytoplasm portion to the cell exterior through the coupled states between the redox of the metal ions and the proton transfer (PT) of the HIm molecule.[3]

Proton conductivity in solids has been widely used as ionic separators in fuel cells.[4, 5] Inorganic protonic conductors, such as β-alumina, sulfate, and phosphate, have been extensively studied over the past decade.[4] Furthermore, an organic perfluorinated polymer (nafion) has attracted considerable attention because of its flexibility and high protonic conductivity, in the order of $\approx 10^{-2}\,S\,cm^{-1}$, even in the low-temperature regions.[5, 6] In contrast, protonic conductors of crystalline molecular materials, such as HIm, urea, acetamide, and pyrimidines, have not achieved comparable success, on account of their low protonic conductivities (10^{-8}–$10^{-13}\,S\,cm^{-1}$).[7] However, the protonic mobility (μ_{H+}) of the molecular material 1*H*-imidazole ($4 \times 10^{-3}\,cm^2\,V^{-1}\,s^{-1}$ at 360 K)[8] was significantly higher than that of a typical inorganic proton conductor, $SrCe_{0.95}Yb_{0.05}O_3$ ($1 \times 10^{-5}\,cm^2\,V^{-1}\,s^{-1}$ at 973 K).[4] This indicates the potential of molecular materials in the development of new protonic conductors that incorporate a proton-conducting path and sufficient protonic carriers into the crystal.

We have been preparing a novel ion–electron coupling system by introducing a supramolecular ionic system, in which ionic motion is possible even within a crystal, to molecular conductors.[9] To achieve high electrical conducting properties, open-shell molecules generated by charge transfer (CT) interactions were necessary to provide highly mobile electronic carriers and to form a partially filled electronic band structure.[10] Salts, such as $(Li^+)_{0.6}$([15]crown-5)[Ni(dmit)$_2$]$_2$ and $(Li^+)_x$([18]crown-6)[Ni(dmit)$_2$]$_2$ (dmit^{2-} = 2-thioxo-1,3-dithiole-4,5-dithiolate), fulfilled these requirements and exhibited high electrical conductivities through a regular [Ni(dmit)$_2$] stack. In addition, the crown ether molecules formed regular ionic channel structures,[11, 12] and the motion of the Li^+ ions within the ionic channel was coupled with the conduction electrons on the [Ni(dmit)$_2$] column. By lowering the temperature, the freezing of the Li^+ motion generated the pinning potential for the conduction electrons, which caused an electronic transition from the metal to the semiconductor with short-range antiferromagnetic interactions. Similarly, protonic conductivity and its freezing in the molecular conductor should couple with the conduction electrons, which can potentially exhibit a unique electronic transition through the proton–electron coupling phenomena.

We selected 2,2′-bi-1*H*-imidazole (H2BIM) derivative as a promising candidate in the formation of a protonic conducting system in the molecular conductor[13, 14] because of three factors: 1) the 1*H*-Imidazole unit of an H2BIM molecule is a functional unit of histidine, which is involved in the protonic transport of cytochrome *c* oxidase, 2) 1*H*-Imidazole shows high protonic mobility, as described above,[3, 8] and 3) H2BIM has multistage PT processes (Scheme 1).[13] The two-step PT processes from H2BIM to 2,2′-bi-1*H*-imidazolium (H4BIM^{2+}) via 2-(2-1*H*-imidazolyl)-1*H*-imidazolium (H3BIM$^+$) allow the 6π–6π electronic structure to be maintained. Since H3BIM$^+$ has three proton-donating amino and one proton-accepting imino sites, the molecule can simultaneously provide protonic carriers and vacant protonic sites. The protonic migration field in the crystal lattice can be provided by the multistage PT character. In addition, H2BIM has a similar molecular shape as the well-known organic donor, tetrathiafulvalene (TTF), which has led to the first molecular metal (TTF)(7,7,8,8-tetracyano-*p*-quinodimethane (TCNQ)).[15] We have previously reported on the CT complex of (H3BIM$^+$)$_2$(TCNQ)$_3$,[14]

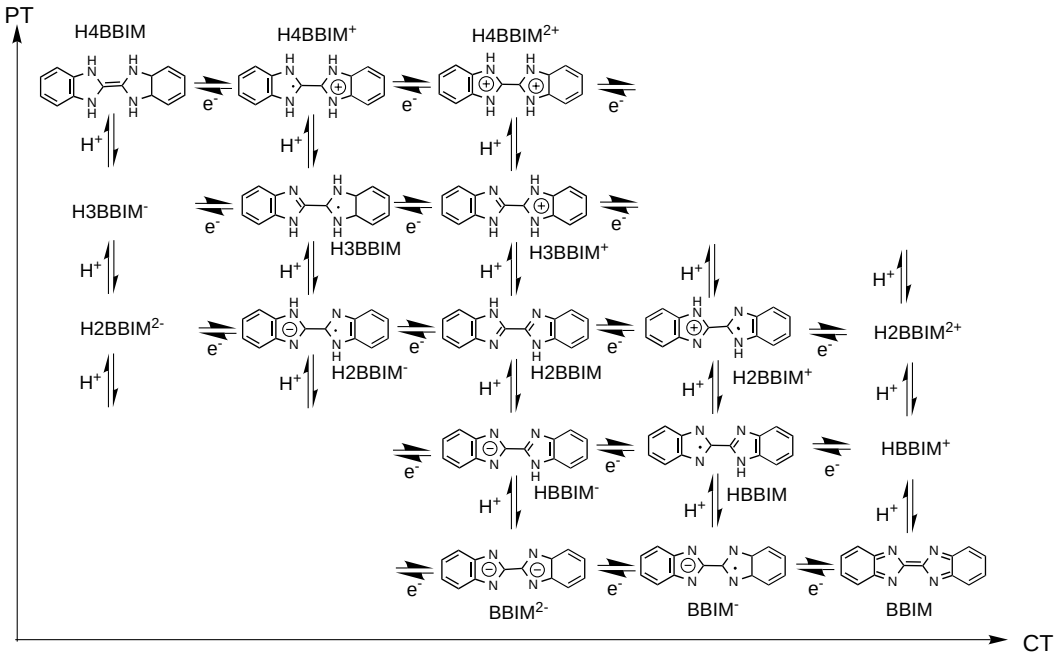

Scheme 1. Proton-transfer and electron-transfer diagram of H2BBIM.

  0947-6539/02/0819-4403 $ 20.00+.50/0

and its notably different crystal structure compared to the uniform segregated stack that is found in (TTF)(TCNQ).[10, 15] Within the crystal, the hydrogen-bonding H3BIM$^+$ dimer units did not form any $\pi-\pi$ stacks, and were arranged normal to the nonuniform trimerized TCNQ stack.[14] Unfortunately, the proton conducting path was not realized in the crystal.[16]

In the present study, we selected 2,2′-bi-1*H*-benzimidazole (H2BBIM) for the construction of our novel proton–electron coupling system.[17] Among the several PT and CT species (Scheme 1), the monocationic 2-(2-1*H*-benzimidazolyl)-1*H*-benzimidazolium (H3BBIM$^+$) was employed for the CT complex formation with TCNQ for the following reasons: 1) the molecular shape and charged state of H3BBIM$^+$ are almost equal to that of the dibenzotetrathiafulvalene cation radical (DBTTF$^+$); the extended π-conjugated system in H3BBIM$^+$ is advantageous in increasing the magnitude of $\pi-\pi$ interactions when they form a stacking structure, 2) from the viewpoint of hard and soft acids and bases (HSAB), H3BBIM$^+$ is a soft base compared to H3BIM$^+$; since a hard acid, such as a proton, forms a stable complex with a hard base, the soft proton-accepting base was advantageous to the PT processes, even as the solid, and 3) the side-by-side steric repulsion at the aromatic hydrogen atoms should prevent the formation of a side-by-side hydrogen-bonding structure, as was observed in (H3BIM$^+$)$_2$(TCNQ)$_3$. The segregated stacking structure has been reported for the completely ionized (DBTTF$^+$)(tetrafluoro-7,7,8,8-tetracyano-*p*-quinodimethane (F_4TCNQ)$^-$) complex.[18] Herein we wish to report on the CT complex of H3BBIM$^+$ with TCNQ, in which the protonic system of H3BBIM$^+$ was strongly coupled with the electronic system of TCNQ.

Results

Preparation of the CT salt: As shown in Scheme 1, the H3BBIM$^+$ cation is involved in the multistep acid dissociation and electron-transfer processes. Each PT or CT process can be evaluated by the redox potential (E) and acid dissociation constant (pK_a), assuming a constant solvation energy. The acid dissociation constant of H3BBIM$^+$ (p$K_a = 2.32$) was roughly two pK_a units lower than that of the parent H3BIM$^+$ (p$K_a = 4.60$).[13] The proton-donating ability of the H3BBIM$^+$ ion was similar in magnitude to that of 2,5-dihydroxy-*p*-benzoquinone (p$K_a = 2.71$).[19] Since the pK_a value of the parent H4BIM^{2+} dication has been estimated to be -0.24,[13] the pK_a of the H4BBIM^{2+} dication should have a negative value.

The H3BBIM$^+$ ion was irreversibly reduced to the corresponding neutral radical with a $6\pi-7\pi$ electronic state at peak potentials of -0.68 V, which was significantly lower than that of TCNQ ($E_r(1) = +0.22$ V). Since 4,4′-dimethylviologen^{2+}, a typical cationic electron acceptor, was reduced to the open-shell $6\pi-7\pi$ and neutral $7\pi-7\pi$ electronic states through a two-step reversible reduction process, at -0.38 V and -0.80 V,[20] the electron-accepting ability of H3BBIM$^+$ was roughly 0.3 V lower than that of the 4,4′-dimethylviologen dication. Therefore, we can safely conclude that the CT process, from the H3BBIM$^+$ cation to TCNQ, can be neglected during the CT complex formation. Only the PT process is sufficient to explain the formation of the CT complex in the following.

Since we did not observe CT complex formation in the electrocrystallization solvent of CH_3CN, because of the deprotonation process from H3BBIM$^+$ to H2BBIM, we can control the PT state of H3BBIM$^+$ during the electrocrystallization procedure. By adjusting the pH of the crystallization solvent to approximately 1.2, at which point H3BBIM$^+$ became the dominant species in the solution, we were able to prepare the (H3BBIM$^+$)(TCNQ)(Cl$^-$)$_{0.5}$(H_2O) (**1**) salt in the CH_3CN/Clark–Lubs buffer solution at pH = 1.2 (20/1).

Crystal structure and CT state: Segregated uniform stacks of H3BBIM$^+$ and TCNQ molecules are observed along the *c* axis (Figure 1). As expected, the extended π-conjugated system of the monovalent H3BBIM$^+$ cation formed a uniform $\pi-\pi$ stacking structure.[18] In addition, the side-by-side arrangement of the regular H3BBIM$^+$ columns formed a channel as a sequence of holes along the *c* axis (dashed circles in Figure 1a). These hydrophilic holes were surrounded by one imino nitrogen and three acidic amino protons of H3BBIM$^+$, and also contained disordered Cl$^-$ ions and H_2O molecules that originated from the buffer solution. The hydrophilic

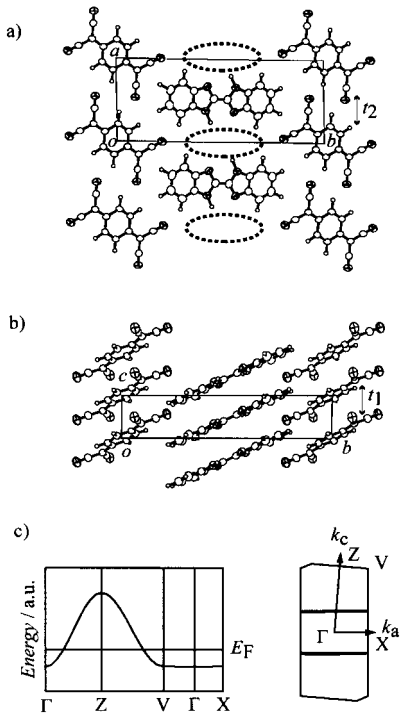

Figure 1. Crystal structure of (H3BBIM$^+$)(TCNQ)(Cl$^-$)$_{0.5}$(H_2O). a) Molecular packing of H3BBIM$^+$ and TCNQ viewed along the *c* axis. The channel-like sequence of pores between the H3BBIM$^+$ stacks are elongated along the c axis (dashed circles). Cl$^-$ ions and H_2O molecules in the channel are omitted in the figure. The transfer integral t_2 corresponds to the interstack interaction along the *a* axis. b) Unit cell viewed along the *a* axis. The transfer integral t_1 corresponds to the intrastack interaction within the TCNQ. c) Energy dispersion and Fermi surface of the LUMO band of the TCNQ stack. The Fermi level (E_F) is assigned for a quarter-filled occupancy of the LUMO band. The *Γ*, Z, V, and X points are [000], [001], [101] and [100], respectively.

0947-6539/02/0819-4404 $ 20.00+.50/0 *Chem. Eur. J.* **2002**, *8*, No. 19

channel, including the disordered Cl^- ions and liquid-like H_2O molecules, provided the proton-conducting path. The amino and imino atoms of $H3BBIM^+$ could not be crystallographically distinguished because of the inversion center located on the $H3BBIM^+$ molecule.

The mean interplanar distances within the TCNQ and the $H3BBIM^+$ stacks were 3.28 Å and 3.45 Å, respectively (Figure 1b). The transfer integral ($t \times 10^{-2}$ eV) within the TCNQ stack ($t_1 = 14.9$) was significantly larger than that of the interstack interaction along the *a* axis ($t_2 = 0.12$). The highly anisotropic intermolecular interactions ($t_1:t_2 = 150:1$) is characteristic of TCNQ-based molecular conductors.[21] For high electronic conductivity on the TCNQ stack, a partially filled LUMO band is necessary. From the stoichiometry, the charge (δ) of each TCNQ molecule was calculated as -0.5, thus the regular TCNQ stack formed a quarter-filled LUMO-band. The δ of TCNQ was also deduced as 0.53 from the bond lengths of TCNQ, c/(b + d) (Table 1).[22] The incomplete band

Table 1. Intramolecular bond lengths of TCNQ in salt **1**, neutral $TCNQ^0$, and fully ionized $TCNQ^-$.

	a	b	c	d
1	1.346(6)	1.430	1.394(6)	1.434
$TCNQ^0$	1.346	1.448	1.374	1.441
$TCNQ^-$	1.373	1.426	1.420	1.416

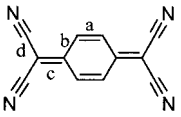

occupancy was confirmed by electronic absorption at 3.2×10^3 cm^{-1} in the UV/Vis-NIR spectra, which corresponded to the intraband CT transition.[23, 24] A highly one-dimensional Fermi surface of the LUMO band was observed in the energy dispersion curve along the k_c direction (Figure 1c), which was also supported by the anisotropy of electrical conductivity (see below). The appearance of the Fermi surface in the band calculation with a tight-binding approximation was consistent with the metallic state of salt **1** at room temperature.

It is possible that the Cl^- ions and H_2O molecules in the channel possess motional freedom, which has been partly supported by preliminary solid-state deuterium NMR measurements.[25] From a room temperature structural analysis, disordered Cl^- and four oxygen sites (O1, O1′, O2, and O2′; herein the prime symbol indicates the atomic sites generated by the inversion center) were observed in the unit cell. The occupancy factors of the Cl^-, O1, and O2 atomic sites were 0.25, 0.25, and 0.25, respectively. Figure 2a shows the one Cl^- and four oxygen atomic sites together with the central C_2N_4 unit of $H3BBIM^+$ along the *c* axis. Each disordered atomic site was nearly planar with a large anisotropic thermal factor (Figure 2a, lower figure).

The oscillation photograph taken at 100 K provided additional information on the disordered Cl^- ions and H_2O molecules within the channel (Figure 2b). A superstructure with $0.5c^*$ periodicity along the *c* axis was observed at 100 K between the Bragg reflections ($l = -1$ and $l = 0$), which should

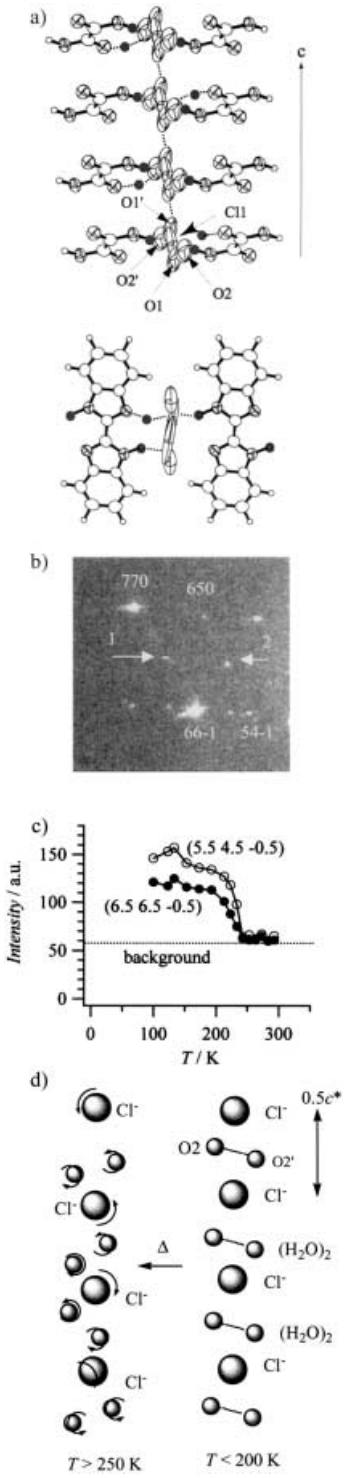

Figure 2. Structure of Cl^- ions and H_2O molecules within the channel. a) Site distribution of the disordered Cl^- ions and H_2O molecules within the channel at 298 K. The Cl^- ionic site is located at the inversion center, while the four disordered oxygen sites O1, O1′, O2, and O2′, in addition to the central C_2N_4 unit of $H3BBIM^+$ molecule, are observed around the Cl^- site. The lower representation is a top view along the channel. The solid circles are a schematic representation of amino protons. b) Oscillation photograph at the reflection region of $l = -1$ and 0 Bragg reflections ($T =$ 100 K). Two spots (1 and 2) correspond to the superstructures of (6.5 6.5 -0.5) and (5.5 4.5 -0.5) reflections, respectively. c) Temperature-dependent intensity change of superstructures (6.5 6.5 -0.5) and (5.5 4.5 -0.5). d) Models of possible $[Cl^- - (H_2O)_2]$ sublattice at $T > 250$ K (left) and $T < 200$ K (right). The semicircular arrows correspond to the thermal motion of Cl^- and H_2O at $T > 250$ K.

mainly reflect the periodicity of Cl^- ions with their large electron density. Figure 2c shows the temperature-dependent intensity variations of the (6.5 6.5 −0.5) and (5.5 4.5 −0.5) superstructures. Diffuse spots or streaks over the background intensity were not observed for temperatures above 250 K. Below 250 K, the intensities of the superstructures continuously increased as the temperature decreased; the intensity was saturated at around 200 K. These superstructures may have originated from the ordering of the Cl^- ions within the channel; thermally disordered Cl^- ions will begin to fix at 240 K, and almost freeze at 200 K. The periodic Cl^- arrangement within the channel also induced the ordering of the H_2O molecules to a form $[Cl^- – (H_2O)_2]$ sublattice, which was confirmed by its vibrational spectra (see below).

In considering the $0.5c^*$ periodicity of Cl^- ions below 250 K, the Cl^- ion at the inversion center occupied every other site along the *c* axis. The nearest-neighbor Cl⁻—O distances (Cl—O1 0.94(4), Cl—O2 1.83(2) Å) were too close to occupy the Cl^- and O atomic sites simultaneously within the same unit cell, whereas the O1—O1′, O1—O2′, and O2—O2′ distances within the original unit were 2.86(3), 2.60(5), and 3.893(1) Å, respectively. In view of the sum of the van der Waals radii of oxygen atoms (O—O 3.04 Å) and the hydrogen-bonding O—O distances (2.4 – 3.0 Å),[26, 27] simultaneous occupation of two oxygen sites in O1—O1′, O1—O2′, or O2—O2′ was a structurally reasonable arrangement. One possible arrangement below 200 K was the alternating occupation of Cl^- ions and H_2O dimers at the O2—O2′ (O1—O1′ or O1 – O2′) atomic site, which then formed a one-dimensional $[Cl^- – (H_2O)_2]$ sublattice along the *c* axis (Figure 2d).

Vibrational spectra: The protonated state of H3BBIM$^+$ in the crystal was evaluated using the vibrational spectra in the frequency range of 1500 – 1700 cm^{-1}. Since broad CT absorption appeared above 1500 cm^{-1}, the NH in-plane bending mode (δ_{NH}) was used to monitor the PT state.[14, 28] As shown by the dashed lines in Figure 3a, salt **1** exhibited three δ_{NH} bands (1636, 1622, and 1604 cm^{-1}), which were consistent with the parent H3BBIM$^+$ (1636, 1624, and 1605 cm^{-1}). In contrast, H2BBIM showed two δ_{NH} absorptions at 1616 and 1584 cm^{-1}, while H4BBIM^{2+} exhibited a single band at 1623 cm^{-1} (Figure 3a). Therefore, H3BBIM$^+$ was the main protonated state in the salt **1**.

The vibrational spectrum of salt **1** measured at 15 K clearly showed the growth of a new band at 1589 cm^{-1} (indicated by an asterisk in Figure 3a), which was possibly attributable to the δ_2-bending mode of the H_2O dimer.[29] The energy of the δ_2-bending mode in $(H_2O)_2$ in an argon matrix has been reported to be 1590 cm^{-1};[29] this is comparable to that observed for salt **1** at low temperatures. The oscillation photograph indicated the formation of a Cl^- superstructure with $0.5c^*$ periodicity below 250 K, which also caused the dimer arrangement of H_2O molecules between the Cl^- sublattice. Since the $0.5c^*$ periodicities of the Cl^- and H_2O dimers were correlated to each other, the formation of the H_2O dimer arrangement also contributed to the intensity of the $0.5c^*$ superstructure. We have assigned this new absorption to the δ_2-bending mode of the H_2O dimer in the $[Cl^- – (H_2O)_2]$ sublattice.

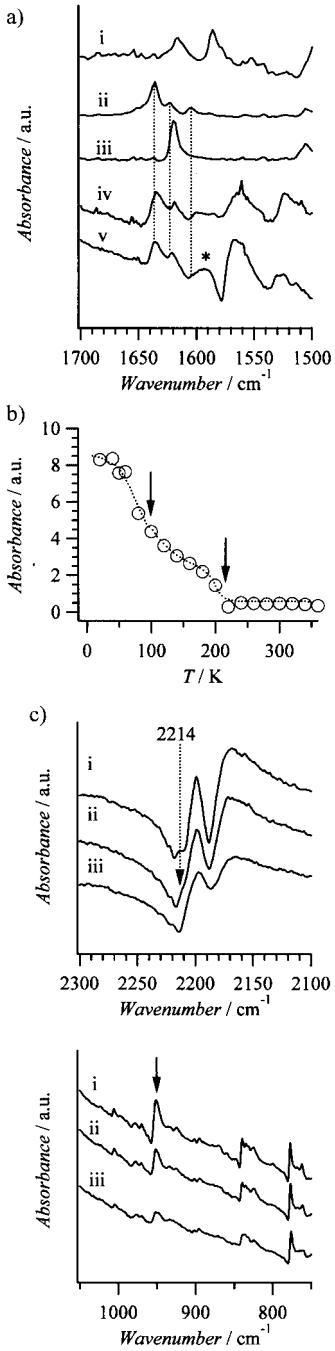

Figure 3. Vibrational spectra of the H2BBIM system in the frequency range from 1500 – 1700 cm^{-1}. a) The N – H in-plane bending-mode (δ_{NH}) of i) H2BBIM, ii) $(H3BBIM^+)(BF_4^-)(H_2O)$, iii) $(H4BBIM^{2+})(BF^-)_2$, iv) $(H3BBIM^+)(TCNQ)(Cl^-)_{0.5}(H_2O)$ (**1**) at 300 K, and v) **1** at 15 K. The asterisk indicates the new absorption at 15 K. The δ_{NH} bands in H3BBIM$^+$ (ii) and **1** are indicated by dashed lines. b) Temperature-dependent intensity changes at 1589 cm^{-1} absorption. Arrows at 220 and 100 K correspond to the disappearance temperature of protonic conductivity and transition temperature to the electronic insulator, respectively. c) Vibrational spectra of TCNQ at the frequency region 2100 – 2300 cm^{-1} (upper) and 750 – 1050 cm^{-1} (lower) at i) 20 K, ii) 150 K, and iii) 270 K. Vibrational a_g modes in TCNQ are observed at 2214 ($\tilde{\nu}_2$) and 951 ($\tilde{\nu}_6$) cm^{-1} (arrows).

The temperature dependence of the vibrational spectra indicated an increase of the $(H_2O)_2$ δ_2-bending band below 200 K (Figure 3b); this temperature is in agreement with that at which the intensity of Cl^- superstructures was saturated.

0947-6539/02/0819-4406 $ 20.00+.50/0 *Chem. Eur. J.* **2002**, *8*, No. 19

One possible explanation for this temperature dependence is the freezing of thermal H_2O motion at around 200 K, at which temperature liquid-like H_2O molecules convert to the $(H_2O)_2$ arrangement at their fixed position within the channel. As mentioned above, a possible occupied state of the disordered H_2O molecules was the alternating arrangement of Cl^- and $(H_2O)_2$ with $0.5\,c^*$ periodicity. At 240 K, the thermal freezing process of heavy Cl^- ions will begin, then at 200 K the lighter H_2O molecules will begin to become fixed at the $(H_2O)_2$ position. An increase of the δ_2-bending absorption at around 100 K indicated the rearrangement of $(H_2O)_2$ from loose O2–O2′ (3.89Å) to tight O1–O1′ (2.86 Å) or O1–O2′ (2.60 Å) within the channel, at which temperature the electronic state can suddenly become highly insulating (see below).

Figure 3c shows the typical vibrational a_g-modes of TCNQ as observed in the IR region. TCNQ exhibited a weak absorption at 20 K (Figure 3c, Spectrum i, $\nu_2 = 2214\ cm^{-1}$), which became a shoulder at 150 K (Figure 3c, Spectrum ii), and unresolved at 270 K (Figure 3c, Spectrum iii). Within the frequency range from 750–1050 cm^{-1}, the $\tilde{\nu}_6$ band was clearly defined at 951 cm^{-1}.[30] Increase in this band was demonstrated by measuring at lower temperatures, namely 270, 150, and 20 K (i) (Figure 3c, Spectra iii, ii, i, respectively). The appearance of these a_g-bands is direct evidence for TCNQ lattice dimerization at low temperatures.[30] Lattice dimerization was strongly associated with the electrical conducting behavior (see below).

Electrical conductivity and magnetic susceptibility: Because of the regular TCNQ stack and the one-dimensional Fermi surface, calculated within tight-binding approximation, salt **1** was expected to have a metallic state. The electrical conductivity at room temperature (σ_{RT}) was found to be 10 $S\,cm^{-1}$ along the stacking *c* axis, while those along the *a* and *b* axes were in the range of $10^{-5}\,S\,cm^{-1}$. The highly anisotropic conductivity was consistent with a one-dimensional band structure.

Temperature-dependent electrical conductivity measurements at ambient pressure showed weakly metallic behavior at temperatures above 250 K (Figure 4, right axis). Within the temperature range from 250 to 100 K, semiconducting behavior was dominant with an activation energy (E_a) of 40 meV, whereas at roughly 100 K, an abrupt transition to an insulating state was observed (Figure 4). The metal–semiconductor transition temperature at 250 K corresponded to the temperature at which the Cl^- superstructure started its growth. Formation of the charged Cl^- sublattice acted as the electron-localization potential for the conduction electrons and influenced the one-dimensional electronic structure of the TCNQ stack. The sublattice formation of the Cl^- ions and the TCNQ lattice dimerization, mentioned earlier, were related to each other mainly through strong Coulomb interactions between the Cl^- ions and the conduction electrons. The abrupt transition to the highly insulating state at 100 K was attributed to the strong electron localization on the TCNQ dimer sites, at which temperature the rearrangement of the $[Cl^- – (H_2O)_2]$ sublattice was possible. Therefore, the electronic transitions of salt **1** were coupled with the $[Cl^- – (H_2O)_2]$ sublattice formation.

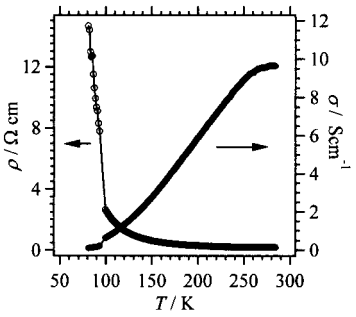

Figure 4. Temperature-dependent electrical resistivity (scale on left) and conductivity (scale on right) of $(H3BBIM^+)(TCNQ)(Cl^-)_{0.5}(H_2O)$.

The magnetic susceptibility (χ_m) of salt **1** at room temperature was 3.6×10^{-4} emu mol^{-1}. The χ_m values gradually increased as the temperature decreased. At around 80 K, a broad maximum was observed (Figure 5). Although electrical conductivity measurements showed an abrupt transition from semiconductor to insulator at 100 K, a magnetic anomaly was not observed at 100 K. Good agreement was observed for the temperature-dependent χ_m behavior below 250 K and the one-dimensional linear Heisenberg antiferromagnetic chain model, with a magnetic exchange energy (J/k_B) of -59 K after subtracting the Curie component ($S = ½$ spin 0.7%).[31] The deviation from the fitting curve above 250 K was attributed to the contribution from metallic Pauli paramagnetism. TCNQ has a charge of -0.5 per molecule in the metallic state, while the conduction electron at low temperature should be localized on the TCNQ dimer site. Short-range antiferromagnetic spin interactions between the $(TCNQ)_2^-$ sites were observed. The temperature-dependent electron-spin resonance (ESR) measurements were also consistent with the static magnetic susceptibility measurements, which did not show evidence of antiferromagnetic ordering or disappearances of spin susceptibility down to 3.8 K.

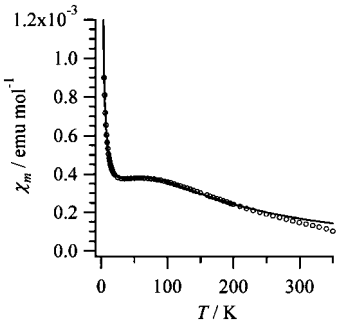

Figure 5. Temperature-dependent molar magnetic susceptibility (χ_m) of $(H3BBIM^+)(TCNQ)(Cl^-)_{0.5}(H_2O)$. The solid line is the fitting curve that uses the one-dimensional linear Heisenberg antiferromagnetic chain model and Curie impurity at the temperature range from 2 to 200 K.

Protonic conductivity: Since the high electrical conductivity of salt **1** caused difficulties in the direct measurement of the

  0947-6539/02/0819-4407 $ 20.00+.50/0

protonic conductivity, a proton-conducting nafion® film was employed as the electron-blocking electrodes for the measurements. Formation of an electric double layer or electrode uniformity at the sample/electrode interface influenced the overall protonic conductivity. The AC impedance method is typically employed for the evaluation of intrinsic protonic conductivity and sample/electrode interface effect.[4] The equivalent circuit of the ion-conducting material was a parallel circuit between the resistance R and capacitance C. The total equivalent circuit for the measuring system, which included the interface effect at the electrode, was a series of circuits between the intrinsic and the sample/electrode circuits (Figure 6a).[4] The R_s (R_e) and C_s (C_e) were the intrinsic

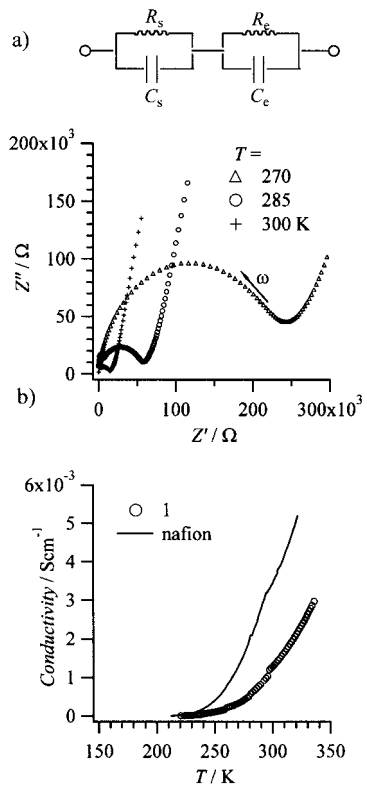

Figure 6. Protonic conductivity of (H3BBIM$^+$)(TCNQ)(Cl$^-$)$_{0.5}$(H$_2$O). a) Resistance (Z') versus reactance (Z'') plots at 300, 285, and 270 K in the frequency (ω) range from 10^2-10^7 Hz. The equivalent circuit for the measuring system is shown. The slanted line at the lower frequency region (right-hand side) caused by the sample/electrode interface effect. b) Temperature-dependent protonic conductivity of the salt **1** (○) and nafion film (——).

(sample/electrode interface) resistance and capacitance, respectively. The overall impedance (Z) was expressed as Equation (1), where Z', Z'' and ω are resistance, reactance, and frequency, respectively.

$$Z = Z' - jZ'' = \frac{R_s}{1 + j\omega C_s R_s} + \frac{R_e}{1 + j\omega C_e R_e} \quad (1)$$

Figure 6a shows the plots of Z' against Z'' at 300, 285, and 270 K in the frequency range from 100 to 1×10^7 Hz. Typical semicircular arc-shaped Z'/Z'' spectra of Debye-type relaxation were observed, which are similar to those observed for typical ionic or protonic conductors.[4–6] Since the rise in the lower frequency region (right-hand side in Figure 6a) can be assigned to sample/electrode interface effects ($R_e - C_e$ term), the protonic resistance (R_s) was estimated from the intercept of the semicircular arc on the Z' axis with Equation (2).[4]

$$\left(Z' - \frac{R_s}{2}\right)^2 + (Z'')^2 = \left(\frac{R_s}{2}\right)^2 \quad (2)$$

The protonic conductivity exhibited by salt **1** was significantly higher than that of ordinary molecular proton-conducting materials, such as 1*H*-imidazole, urea, acetamide, pyrimidines, etc.[7] One explanation for the high protonic conductivity is the liquid-like environment within the channel and the large number of vacant protonic sites that are provided by H_2O and the imino nitrogen of the H3BBIM$^+$ molecule within the channel. In the hydrogen-bonded crystalline materials, proton transfer followed by the reorientation of core molecules is necessary to realize the protonic conductivity throughout the hydrogen-bonding network. On the other hand, high protonic conductivity in nafion film was dominated by the existence of liquid-like H_2O molecules within the film, where molecular motion of H_2O assisted the protonic transport; conversely, the motional freezing of the H_2O molecules diminished the protonic conduction of the nafion® film. Since the thermally fluctuating liquid-like H_2O molecules within the channel were in a comparable environment to that in the nafion® film, the conducting mechanism in salt **1** was similar to that of the nafion® film. The motional freezing of Cl$^-$ ions and H_2O molecules, upon [Cl$^-$ – (H$_2$O)$_2$] sublattice formation, suppressed the protonic conductivity at around 200 K. However, it is important to note that we cannot exclude contributions from protonic conductivity through the crystal grain boundary in a powder sample.

Discussion

Proton – electron coupling was observed between the proton-conducting channel formed by H3BBIM$^+$ stacks and electron-conducting TCNQ stacks. Particularly the formation of protonic (ionic) lattices localizes the conduction electrons on TCNQ stacks. Salt **1** exhibited three types of temperature-dependent electronic states: metal ($T > 250$ K), semiconductor ($250 > T > 100$ K), and insulator ($T < 100$ K).

The gradual metal – semiconductor transition at 250 K seemed to occur through a similar mechanism to that found in (Li$^+$)$_{0.6}$([15]crown-5)[Ni(dmit)$_2$]$_2$ and (Li$^+$)$_x$([18]crown-6)[Ni(dmit)$_2$]$_2$ salts, which has been explained in terms of Li$^+$ motion and its freezing within the ionic channel by lowering the temperature.[11, 12] The freezing of ionic motion in the channel caused a static disorder and generated a pinning potential for conduction electrons in the one-dimensional LUMO band of [Ni(dmit)$_2$]. In the case of salt **1**, the freezing of Cl$^-$ ions with a periodicity of 0.5 c* below 250 K changed the electrical conductivity from metal to semiconductor. The magnetic susceptibility of salt **1** also showed a gradual transition from the metallic Pauli paramagnetism to a one-dimensional linear Heisenberg antiferromagnetic semiconductor at 250 K. The appearance of vibrational a_g bands

0947-6539/02/0819-4408 $ 20.00+.50/0 *Chem. Eur. J.* **2002**, *8*, No. 19

demonstrated dimerization in the regular TCNQ stack below 250 K. The $0.5c^*$ Cl^- ionic lattice generated the periodic electron-localization potential for the conduction electrons, which should be the origin of the gradual metal–semiconductor transition at 250 K.

At temperatures below 250 K, short-range antiferromagnetic spin interaction was expected between the conduction electrons. The appearance of a_g modes in the vibrational spectra suggested that the conduction electrons were weakly localized on the TCNQ dimer sites. The small activation energy (40 meV) for the electrical conductivity in the temperature range from 250–100 K was consistent with the weak localization property and short-range magnetic interaction. Lowering of the temperature caused the thermal freezing of heavy Cl^- ions at 250 K, and upon further cooling, the lighter H_2O molecules gradually became fixed at H_2O dimer positions. Complete formation of the $[Cl^- – (H_2O)_2]$ sublattice at around 200 K effectively disabled proton conductivity.

The semiconductor–insulator transition at 100 K was caused by strong electron localization on the $(TCNQ)_2^-$ units, which are associated with the rearrangement of the $[Cl^- – (H_2O)_2]$ sublattice. If the electronic transition at 100 K was related to the formation of a charge density wave (CDW), magnetic susceptibility should drop discontinuously at around 100 K. The continuous temperature-dependent magnetic susceptibility suggested a gradual increase of the localization property of the conduction electrons on the $(TCNQ)_2$ sites. Similar temperature-dependent electronic conductivity and magnetic susceptibility have been reported for (*N*-methyl-*N*-ethyl-morpholinium (MEM^+))$(TCNQ)_2$, which exhibited spin-Peierls and Mott transitions at 19 and 340 K, respectively.[32–34] Below 340 K, the regular TCNQ stack in $(MEM^+)(TCNQ)_2$ was distorted as the $(TCNQ)_2^-$ dimer lattice, at which point each electron was localized on the $(TCNQ)_2^-$ site on account of electronic repulsive interactions (Mott transition). The spin-Peierls transition at 19 K was caused by TCNQ tetramerization of $[(TCNQ)_2^- – (TCNQ)_2^-]$, and the magnetic spins disappeared as a result of the formation of a spin singlet state between the $(TCNQ)_2^-$ sites. The magnetic susceptibility of $(MEM^+)(TCNQ)_2$ in the temperature range from 19–400 K followed the one-dimensional liner Heisenberg chain model without magnetic anomaly at around 340 K.[33] In terms of temperature-dependent electrical conductivity, magnetic susceptibility, and lattice dimerization, the electronic transition at 100 K of salt **1** was similar to the Mott transition found for $(MEM^+)(TCNQ)_2$.

Conclusion

The multistage proton-transfer system of 2-(2-1*H*-benzimidazolyl)-1*H*-benzimidazolium ($H3BBIM^+$) was incorporated into the molecular conductor of $(H3BBIM^+)(TCNQ)(Cl^-)_{0.5}(H_2O)$ through a pH-controlling electrocrystallization method. The regular TCNQ stack formed a one-dimensional electronic system. Furthermore, the channel-like proton-conducting sequence of pores was formed by the side-by-side arrangement of the regular $H3BBIM^+$ columns, in which disordered Cl^- ions and H_2O molecules filled the holes at room temperature. Three types of electronic states were observed: Above 250 K, metallic electronic state with conductivity of 10 $S\,cm^{-1}$ coexisted with protonic conductivity up to 1×10^{-3} $S\,cm^{-1}$. Through the channel-like pore, the protonic conductivity was first realized in the molecular conductor. The magnetic behavior gradually changed from a Pauli paramagnetic spin system to a one-dimensional linear Heisenberg antiferromagnetic chain at 250 K. In the temperature range from 100 to 250 K the salt showed semiconducting properties with short-range antiferromagnetic interactions as a result of the formation of the $[Cl^- – (H_2O)_2]$ sublattice. The conduction electrons were weakly localized by the generation of the pinning potential of the Cl^- sublattice with $0.5c^*$ periodicity at 250 K. As a result of the formation of the $[Cl^- – (H_2O)_2]$ sublattice, protonic conductivity disappeared below 200 K. Weak dimerization of TCNQ was suggested by vibrational spectroscopy studies. Below 100 K, an insulated state was observed. Strong localization of the conduction electrons on the $(TCNQ)_2^-$ dimer sites caused a Mott transition as a result of an the electron-repulsive interaction, which was induced by the $[Cl^- – (H_2O)_2]$ sublattices.

The dynamic property of a protonic (or ionic) lattice influences the conduction electrons. In the present study, the metal–semiconductor and semiconductor–insulator transitions were associated with the freezing and melting processes of $[Cl^- – (H_2O)_2]$ sublattice through the proton–electron coupling. Mixed protonic and electronic conductors in the molecular system are important in the field of technological applications, such as batteries, sensors, and electrochromic displays.[35–37]

Experimental Section

General: Infrared (IR, 400–7600 cm^{-1}) spectra were measured as KBr pellets with a Perkin-Elmer Spectrum 2000 spectrophotometer (resolution: 1 cm^{-1}). The temperature-dependent IR spectra were measured with a cryogenic refrigerating system (Daikin UV 202A) in the temperature range from 15 to 300 K. The UV/Vis-NIR spectra (350–3200 nm) were measured as KBr pellets with a Perkin-Elmer lambda-19 spectrophotometer (resolution: 8 nm). Acid dissociation constants and redox potentials were measured by standard titration and cyclic voltammetry (CV) methods, respectively, as described in our previous paper.[14] *N*,*N*′-Dimethylformamide (DMF) was distilled twice in vacuo prior to use. The ionic strength (0.1 M $NaBF_4$) and temperature (22 ± 1 °C) were fixed during the titration in DMF–H_2O (7:3). The redox potentials were measured in DMF with an Ag/AgCl reference electrode (0.1 M nBu_4NBF_4, Pt working and counter electrodes).

Crystal preparation: 2,2′-Bi-1*H*-benzimidazole (H2BBIM) was prepared by the condensation reaction of *o*-phenylenediamine and oxamide in ethylene glycol (fine yellow needles, m.p. > 350 °C).[38] The supporting electrolyte of $(H3BBIM^+)(I^-)$ was prepared from H2BBIM and hydroiodic acid (yellow powder, m.p. > 400 °C). $(H3BBIM^+)(BF_4^-)(H_2O)$ and $(H4BBIM^{2+})(BF_4^-)_2$ were obtained with similar procedures.

Single crystals of $(H3BBIM^+)(TCNQ)(Cl^-)_{0.5}(H_2O)$ (**1**) were prepared by electrocrystallization of TCNQ and $(H3BBIM^+)(I^-)$. The crystallization solvent, CH_3CN, was distilled over CaH_2 prior to use. Single crystals were grown from a mixed solvent system (CH_3CN/buffer solution 20:1). Clark–Lubs buffer solution with a pH of 1.2 was prepared by mixing HCl and KCl as an aqueous solution. Salt **1** was obtained as black needles after two weeks of electrocrystallization. M.p. 300 °C (decomp); elemental analysis calcd (%) for $C_{26}H_{17}N_8OCl_{0.5}$ (475.2): C 65.73, H 3.58, N 23.59, O 3.79, Cl 3.74; found: C 65.68, H 3.51, N 23.31, O 3.07, Cl, 4.29.

  0947-6539/02/0819-4409 $ 20.00+.50/0

Crystal structural analysis: Crystal data of salt **1** was collected on a Rigaku AFC-7R diffractometer with $Mo_{K\alpha}$ ($\lambda = 0.71073$ Å) radiation at 296 K and a graphite monochromator. The structures were solved and refined with the Crystal Structure software package.[39] Structure refinements were performed with a full-matrix least-squares method on F^2. Parameters were refined by the anisotropic temperature factors, except for hydrogen atoms. Table 2 summarizes the crystal data of salt **1**. Temperature-dependent oscillation photographs were obtained with an imaging plate (R-Axis Rapid) equipped with a liquid nitrogen cooling system. CCDC-181926 contains the supplementary crystallographic data for this paper. These data can be obtained free of charge via www.ccdc.cam.ac.uk/conts/retrieving.html (or from the Cambridge Crystallographic Data Centre, 12 Union Road, Cambridge CB21EZ, UK; fax: (+44) 1223-336033; or deposit@ccdc.cam.uk).

Table 2. Crystal data, data collection, and reduction parameters of salt **1**.

	1
formula	$C_{26}H_{17}ON_8Cl_{0.5}$
M_r	475.20
crystal system	triclinic
space group	$P\bar{1}$
crystal size [mm^3]	$0.6 \times 0.1 \times 0.1$
a [Å]	7.676(1)
b [Å]	19.050(4)
c [Å]	3.894(1)
α [°]	91.36(2)
β [°]	94.92(2)
γ [°]	88.31(2)
V [Å^3]	566.9(2)
Z	1
T [K]	298
ρ_{calcd} [g cm^{-3}]	1.392
μ [cm^{-1}]	1.48
data measured	2782
data independent	2776
data observed	1292
R[a]	0.065
$R_w(F^2)$[a]	0.098
GOF	1.15

[a] $R = \Sigma||F_o| - |F_c||/\Sigma|F_o|$ and $R_w = (\Sigma\omega|F_o| - |F_c|)^2/\Sigma\omega F_o^2)^{1/2}$.

Transport measurements: Temperature-dependent electrical conductivity of salt **1** was measured by the standard DC four-probe method along the c axis and by the two-probe method along the a and b axes. Electrical contacts between gold wire (diameter: 10 μm) and the crystals were made with carbon paste (Dotite XC-12). Temperature-dependent protonic conductivity (150–340 K) was measured by the AC impedance method in the frequency range from 100 to 10×10^6 Hz with an impedance analyzer (HP 4194 A). The compressed pellet, with a diameter of 3 mm, was enclosed by a Teflon ring in order to avoid short circuits, and which was sandwiched by proton-conducting nafion® 117 (Aldrich Co Ltd.). The sample was clamped by metal electrodes, and was inserted into a cryogenic refrigerating system (Daikin PS24SS). The conductivity was measured in vacuo ($< 10^{-3}$ Torr).

Magnetic measurements: The temperature-dependent magnetic susceptibility was measured with a SQUID magnetometer (Quantum Design Model MPMS-5) for polycrystalline samples. The applied magnetic field was 1 T for all measurements.

Transfer integral and band structural calculations: The transfer integrals (t) and band structures were calculated within the tight-binding approximation by means of the extended Hückel molecular orbital calculation based on the crystal structural data.[40] The LUMO of the TCNQ molecule was used as the basis function. The semiempirical parameters for the Slater-type atomic orbitals were used. The t values between each pair of molecules were assumed to be proportional to the overlap integral (s), $t = Es$, where E is a constant at -10.0 eV. The LUMO band of TCNQ in salt **1** was assumed to be quarter-filled.

Acknowledgements

This work was partly supported by a Grant-in-Aid for Science Research from the Ministry of Education, Culture, Sports, Science, and Technology of Japan. The authors thank Dr. M. Wakeshima and Prof. Y. Hinatsu for the use of the SQUID magnetometer.

[1] a) B. Albert, D. Bray, A. Johnson, J. Lewis, M. Raff, K. Roberts, P. Walter, *Molecular Biology of the Cell*, Garland Publishing Inc., New York, **1994**; b) L. Stryer, *Biochemistry*, Freeman, New York, **1995**.
[2] a) R. E. Blankenship, *Anoxygenic Photosynthetic Bacteria. Advances in Photosynthesis Vol. 2*, Kluwer, New York, **1996**; b) D. R. Ort, *Oxygenic Photosynthesis; The Light Reactions; Advances in Photosynthesis Vol. 4*, Kluwer, New York, **1996**.
[3] a) P. J. P. Williams, *Nature* **1995**, *378*, 643; b) S. Iwata, C. Ostermeler, B. Ludwig, H. Michel, *Nature* **1995**, *376*, 660.
[4] *Proton Conductors, solids, membranes and gels materials and devices* (Ed.: P. Colomban), Cambridge University Press, Cambridge, **1992**.
[5] F. M. Gray, *Polymer Electrolyte*, RSC, Cambridge, **1997**.
[6] a) R. A. Wallace, *J. Appl. Phys.* **1971**, *42*, 3121; b) R. C. Slade, A. Hardwick, P. G. Dickens, *Solid State Ionics* **1983**, *9–10*, 1093.
[7] L. Glasser, *Chem. Rev.* **1975**, *75*, 21.
[8] A. Kawada, A. R. McGhie, M. M. Labes, *J. Chem. Phys.* **1969**, *52*, 3121.
[9] a) T. Akutagawa, T. Nakamura, A. E. Underhill, T. Inabe, *J. Mater. Chem.* **1996**, *7*, 135; b) T. Akutagawa, T. Nakamura, T. Inabe, A. E. Underhill, *Thin Solid Films* **1998**, *331*, 264; c) T. Akutagawa, Y. Nezu, T. Hasegawa, T. Nakamura, K. Sugiura, Y. Sakata, T. Inabe, A. E. Underhill, *Chem. Commun.* **1998**, 2599; d) T. Akutagawa, T. Hasegawa, T. Nakamura, T. Inabe, K. Sugiura, Y. Sakata, A. E. Underhill, *Synth. Met.* **1999**, *102*, 1747; e) T. Akutagawa, T. Nakamura, *Coord. Chem. Rev.* **2000**, *198*, 297; f) T. Akutagawa, T. Hasegawa, T. Nakamura, S. Takeda, T. Inabe, K. Sugiura, Y. Sakata, A. E. Underhill, *Inorg. Chem.* **2000**, *39*, 2645.
[10] a) D. O. Cowan, *New Aspects of Organic Chemistry* (Eds.: Z. Yoshida, T. Shiba, Y. Oshiro), Kodansha, Tokyo, **1989**; b) *Organic Conductors* (Ed.: J.-P. Farges), Marcel Dekker, New York, **1994**; c) *Handbook of Organic Conductive Molecules and Polymers Vol. 1* (Ed.: H. S. Nalwa), Wiley, New York, **1997**; d) J. M. Williams, J. R. Ferraro, R. J. Thorn, K. D. Carlson, U. Geiser, H. H. Wang, A. M. Kini, M. -H. Whangbo, *Organic Superconductors* (Ed.: R. N. Grimes), Prentice-Hall, New Jersey, **1992**; e) T. Ishiguro, K. Yamaji, G. Saito, *Organic Superconductors*, 2nd ed., Springer, New York, **1998**.
[11] T. Nakamura, T. Akutagawa, K. Honda, A. E. Underhill, A. T. Coomber, R. H. Friend, *Nature* **1998**, *394*, 159.
[12] T. Akutagawa, T. Hasegawa, T. Nakamura, S. Takeda, K. Sugiura, Y. Sakata, T. Inabe, A. E. Underhill, *Chem. Eur. J.* **2001**, *7*, 4902.
[13] T. Akutagawa, G. Saito, *Bull. Chem. Soc. Jpn.* **1995**, *68*, 1753.
[14] T. Akutagawa, G. Saito, M. Kusunoki, K. Sakaguchi, *Bull. Chem. Soc. Jpn.* **1996**, *69*, 2487.
[15] a) J. P. Ferraris, D. O. Cowan, V. Walatka, J. H. Perlstein, *J. Am. Chem. Soc.* **1973**, *95*, 498; b) L. B. Coleman, M. J. Cohen, D. J. Sandman, F. G. Yamagishi, A. F. Garito, A. J. Heeger, *Solid State Commun.* **1973**, *12*, 1125.
[16] Recently, the protonic channel structure of the [18]crown-6 array in a CT salt has been reported; however, its protonic conductivity has not been evaluated yet. S. Rashid, S. Turner, P. Day, M. E. Light, M. B. Hursthouse, S. Firth, R. J. H. Clark, *Chem. Commun.* **2001**, 1462.
[17] a) T. Akutagawa, G. Saito, H. Yamochi, M. Kusunoki, K. Sakaguchi, *Synth. Met.* **1995**, *69*, 591; b) T. Akutagawa, G. Saito, T. Nakamura, K. Sakaguchi, M. Kusunoki, *Mol. Cryst. Liq. Cryst.* **1996**, *276*, 257.
[18] T. J. Emge, W. A. Bryden, M. Wiygul, D. O. Cowan, T. J. Kistenmacher, *J. Chem. Phys.* **1982**, *77*, 3188.
[19] G. Kortüm, W. Vogel, K. Andrussow, *Dissociation Constants of Organic Acid in Aquaeous Solution*, Butterworths, London, **1961**.
[20] P. M. S. Monk, *The Viologens*, Wiley, Chichester, **1998**.
[21] a) A. J. Berlinsky, J. F. Carolan, L. Weiler, *Solid State Commun.* **1974**, *15*, 795; b) F. Herman, D. R. Salahub, R. P. Messmer, *Phys. Rev. B* **1977**, *16*, 2453.

  0947-6539/02/0819-4410 $ 20.00+.50/0

[22] a) P. S. Flandoris, D. Chasseau, *Acta. Crystallogr. Sect. B* **1977**, *33*, 2744; b) T. J. Kistenmacher, T. J. Emge, A. N. Bloch, D. O. Cowan, *Acta. Crystallogr. Sect B* **1982**, *38*, 1193.
[23] *Semiconductors and Semimetals*, *Highly Conducting Quasi-One-Dimensional Organic Crystals* (Ed.: E. Conwell), Academic Press, New York, **1988**.
[24] a) J. B. Torrance, B. A. Scott, B. Welber, F. B. Kaufman, P. E. Seiden, *Phys. Rev. B* **1979**, *19*, 730; b) J. B. Torrance, *Acc. Chem. Res.* **1979**, *12*, 79.
[25] S. Takeda, unpublished results.
[26] A. Bondi, *J. Phys. Chem.* **1964**, *68*, 441.
[27] a) G. A. Jeffrey, W. Saenger, *Hydrogen Bonding in Biological Structures*, Springer-Verlag, Berlin, **1991**; b) S. Scheiner, *Hydrogen Bonding*, *Theoretical Perspective* (Ed.: D. G. Truhlar), Oxford University Press, New York, **1997**; c) G. A. Jeffrey, *An Introduction to Hydrogen Bonding* (Ed.: D. G. Truhlar), Oxford University Press, New York, **1997**.
[28] D. Boinnard, P. Cassoux, V. Petrouleas, J. M. Savariault, J. P. Tuchagues, *Inorg. Chem.* **1990**, *29*, 4114.
[29] a) R. D. Amos, *Chem. Phys.* **1986**, *104*, 145; b) E. L. Woodbridge, T. Tso, P. M. McGrath, W. J. Hehre, K. C. Lee, *J. Chem. Phys.* **1986**, *85*, 6991.
[30] M. Meneghetti, A. Girlando, C. Pecile, *J. Chem. Phys.* **1985**, *83*, 3134
[31] J. C. Bonner, M. E. Fisher, *Phys. Rev. A* **1964**, *3*, 640.
[32] S. Huizinga, J. Kommandeur, G. A. Sawatzky, K. Kopinga, W. J. M. Jonge, *Quasi One-Dimensional Conductor II* (Eds.: S. Barisic, S. Bjelis, J. R. Cooper, B. Leontic), Springer-Verlag, Berlin, **1979**, p. 45.
[33] B. Bodegom, B. C. Larson, H. A. Mook, *Phys Rev. B* **1981**, *24*, 1520.
[34] N. F. Mott, *METAL-INSULATOR TRANSITIONS*, Taylor & Francis, **1990**.
[35] C. Barthet, M. Guglielmi, *J. Electro. Chem.* **1995**, *388*, 35.
[36] P. Novak, Z. Q. Shan, R. Bjorklund, *J. Electro. Chem.* **1987**, *134*, 1341.
[37] Z. Gao, B. Chen, M. Zi, *J. Chem. Soc. Chem. Commun.* **1993**, 675.
[38] M. S. Hadad, D. H. Hendrickson, *Inorg. Chem.* **1978**, *17*, 2622; b) B. F. Fieselmann, D. N. Hendrickson, G. D. Stucky, *Inorg. Chem.* **1978**, *17*, 2078.
[39] Crystal Structure: Single crystal structure analysis software. Ver. 1.0, **2000**. Rigaku Corporation and Molecular Structure Corporation For Ortep drawings, see: L. J. Farrugia, *J. Appl. Crystallogr.* **1997**, *32*, 565.
[40] a) T. Mori, A. Kobayashi, Y. Sasaki, H. Kobayashi, G. Saito, H. Inokuchi, *Bull. Chem. Soc. Jpn.* **1984**, *57*, 627; b) R. H. Summerville, R. J. Hoffmann, *J. Am. Chem. Soc.* **1976**, *98*, 7240.

Received: March 22, 2002 [F3965]

  0947-6539/02/0819-4411 $ 20.00+.50/0